ADVANCES IN ATMOSPHERIC SCIENCES, VOL. 30, NO. 5, 2013, 1373–1386

Effect of Implementing Ecosystem Functional Type Data in a Mesoscale Climate Model

Seung-Jae LEE*[1], E. Hugo BERBERY[2], and Domingo ALCARAZ-SEGURA[3]

[1]*Complex Systems Science Laboratory, Department of Landscape Architecture and Rural Systems Engineering, Seoul National University, Seoul, Korea*

[2]*Department of Atmospheric and Oceanic Science, University of Maryland, College Park, Maryland, U. S. A.*

[3]*Department of Botany, University of Granada, Granada, Spain*

(Received 7 July 2012; revised 7 December 2012; accepted 10 December 2012)

ABSTRACT

In this paper, we introduce a new concept of land-surface state representation for southern South America, which is based on "functional" attributes of vegetation, and implement a new land-cover (Ecosystem Functional Type, hereafter EFT) dataset in the Weather and Research Forecasting (WRF) model. We found that the EFT data enabled us to deal with functional attributes of vegetation and time-variant features more easily than the default land-cover data in the WRF. In order to explore the usefulness of the EFT data in simulations of surface and atmospheric variables, numerical simulations of the WRF model, using both the US Geological Survey (USGS) and the EFT data, were conducted over the La Plata Basin in South America for the austral spring of 1998 and compared with observations. Results showed that the model simulations were sensitive to the lower boundary conditions and that the use of the EFT data improved the climate simulation of 2-m temperature and precipitation, implying the need for this type of information to be included in numerical climate models.

Key words: Ecosystem Functional Type, WRF, land cover, climate simulation

Citation: Lee, S.-J., E. H. Berbery, and D. Alcaraz-Segura, 2013: Effect of implementing ecosystem functional type data in a mesoscale climate model. *Adv. Atmos. Sci.*, **30**(5), 1373–1386, doi: 10.1007/s00376-012-2143-3.

1. Introduction

In land–atmosphere interactions that involve exchange of the heat, moisture, and momentum between them, vegetation provides important information to establish the partitioning of surface-sensible and latent heat fluxes, and affects the near-surface mass and wind variables. Values of 2-m temperature, 2-m specific humidity, and 10-m wind are related to vegetation characteristics such as albedo, roughness length, leaf area index, vegetation fraction, and others. Influences of vegetation on the near-surface atmosphere are transferred to the planetary boundary layer and even to higher levels in the free atmosphere through turbulence processes and large-scale atmospheric circulations. Hence, inaccurate information on vegetation can give rise to biases in a model simulation, particularly for near-surface, boundary layer, and eventually the entire atmosphere. Therefore, it is hypothesized that the realistic specification of land-surface characteristics is important for the optimal performance of the numerical model.

Several efforts have been made to replace the existing land-cover data, which were defined for relatively short periods, with recent satellite-derived land-cover data in numerical models. Those efforts were carried out in state-of-the-art numerical models such as the Weather and Research Forecasting (WRF) model. For example, the WRF model uses 17-category Moderate Resolution Imaging Spectroradiometer (MODIS) land-

*Corresponding author: Seung-Jae LEE, seungjaelee@snu.ac.kr

cover data in addition to the traditional 24-category US Geological Survey (USGS) land-cover data.

However, both USGS and MODIS datasets are based on a land-cover classification mainly dictated by "structural" attributes of vegetation, and have a high inertia to rapid environmental changes, for example, changes in land cover due to forest fires or in vegetation health due to insect infestations and droughts. To overcome this drawback, Paruelo et al. (2001) and Alcaraz-Segura et al. (2013) proposed a new land-cover classification based on ecosystem processes, called ecosystem functional types (EFT). The EFTs are patches of the land surface with similar carbon gain dynamics and, hence, are entirely based on "functional" attributes of vegetation describing the exchange of energy and matter between the land surface and the overlying atmosphere.Since EFTs can be updated yearly, they allow to deal more effectively with the time-variant features of the land cover, which otherwise cannot be detected using the time-fixed USGS land-cover types.

Because the EFT dataset has not yet been incorporated in any numerical weather or climate models, the primary objectives of this study were to implement it in the WRF model as a new terrestrial boundary condition and to estimate its impact on the climate and hydrology of the region. To fulfill these objectives, numerical simulations of the WRF model using both USGS and EFT data, were carried out for the austral spring of 1998 and compared with observational data. As a first step, the EFTs were defined regionally, not globally. Therefore, rather than providing a new global land-cover map, the present study focused on southern South America region that has been subject to significant land-cover changes since the European settlement, particularly in recent decades. The final objective of this work was to investigate the physical mechanisms by which regional land-cover changes gave rise to changes in regional precipitation.

In section 2, the WRF model is introduced and discussed briefly, along with a description of the EFT data. Section 3 presents results of model simulations and their analysis for surface prognostic and diagnostic variables. In section 4, the model simulations are compared with observational data, and section 5 summarizes the work of this paper and presents the conclusions.

2. Model and data

2.1 *The WRF model configuration*

The WRF modeling system (Advanced Research WRF) is a nonhydrostatic and primitive-equation model with state-of-the-art physics options to parameterize subgrid-scale processes and multiple nesting capabilities, in order to increase the resolution over an area of interest (Michalakes et al., 2001). Since its development, this model has been widely used as a community numerical model and applied in many fields including weather forecasting, climate simulations, and air pollution studies. It is suitable for use in a broad range of applications across scales ranging from meters to thousands of kilometers. The Advanced Research WRF, version 3.1.1, was used in this study. Figure 1 shows the configurations of the model domain and the mother domain, which cover the southern South America and the southwestern Atlantic Ocean. The Andes mountain range is located along the west coast and its average height is about 4 km. The Brazilian Highlands along the central east coast and relatively low lands were formed between the two high terrain features. The boundaries of the La Plata Basin (LPB) are also indicated in the figure.

The grid interval for the mother (nested) domain was 36 km (12 km), with 27 vertical levels from the surface to a height of 10 hPa. National Centers for Environmental Prediction (NCEP) / National Center for Atmospheric Research (NCAR) Reanalysis data (Kalnay et al., 1996) were used for initial and 6-hourly boundary conditions. We used a 180-s time step on the coarse-grid domain, with intervals of progressively shorter time steps on the inner grid.

In the WRF model, numerical simulation of precipitation is very sensitive to the choice of model physical parameterizations. Lee (2010) conducted diverse numerical experiments and suggested an optimal combi-

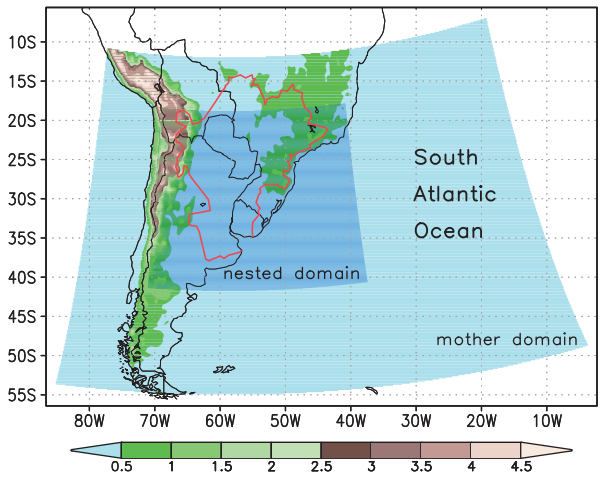

Fig. 1. Domain configuration of the WRF model used in this study. Mother and nested domains have horizontal resolutions of 30 and 10 km, respectively. Contour intervals for topography are indicated at the bottom (units: km).

nation of the model physical processes over southern South America. In our experiment, we adopted that combination, which consisted of the Dudhia shortwave radiation scheme (Dudhia, 1989), the RRTM longwave schemes (Mlawer et al., 1997), the Noah land-surface model (Chen and Dudhia, 2001), the Mellor–Yamada–Janjić boundary layer scheme (Janjić, 1990, 1996, 2002), the Monin–Obukhov–Janjić surface layer scheme (Janjić, 1996, 2002), the Betts–Miller–Janjićcumulus scheme (Janjić, 1994, 2000), and the WRF Single Moment six-class microphysics (Hong and Lim, 2006).

2.2 *Land-cover data and experimental design*

The WRF model has two default land-cover datasets. The first one is based on the USGS global 1-km land-cover map (Anderson et al., 1976) produced from the National Oceanic and Atmospheric Administration (NOAA)'s Advanced Very High Resolution Radiometer (AVHRR) measurements (Loveland and Belward, 1997) from 1992 to 1993. Surface properties such as vegetation and soil moisture data were prescribed following 24 unique USGS land-use categories with different physical properties, including surface albedo, moisture availability, emissivity, and roughness values assigned to each category. The second one is based on data from the National Aeronautics and Space Administration (NASA)'s MODIS measurements and was implemented by Yucel (2006). The MODIS land-cover dataset had 17 USGS land-cover types, which were translated from the International Geosphere–Biosphere Program (IGBP) classes. Both the AVHRR and the MODIS datasets were main based on the "structural" attributes of vegetation.

Alcaraz-Segura et al. (2013) described the concept of EFTs based on "functional" attributes of vegetation related to the carbon gains dynamics. In this work, we implemented the EFTs in the WRF model for southern South America, to show that they can be used as a new classification of land cover. Sixty-four EFTs were identified using three descriptors of carbon gain dynamics derived from the seasonal curves of Normalized Difference Vegetation Index (NDVI), a surrogate of primary production. These three descriptors of carbon gain dynamics were annual mean (estimator of primary production), seasonal coefficient of variation (indicator of seasonality), and date of maximum NDVI (descriptor of phenology) (Alcaraz-Segura et al., 2013). For this,

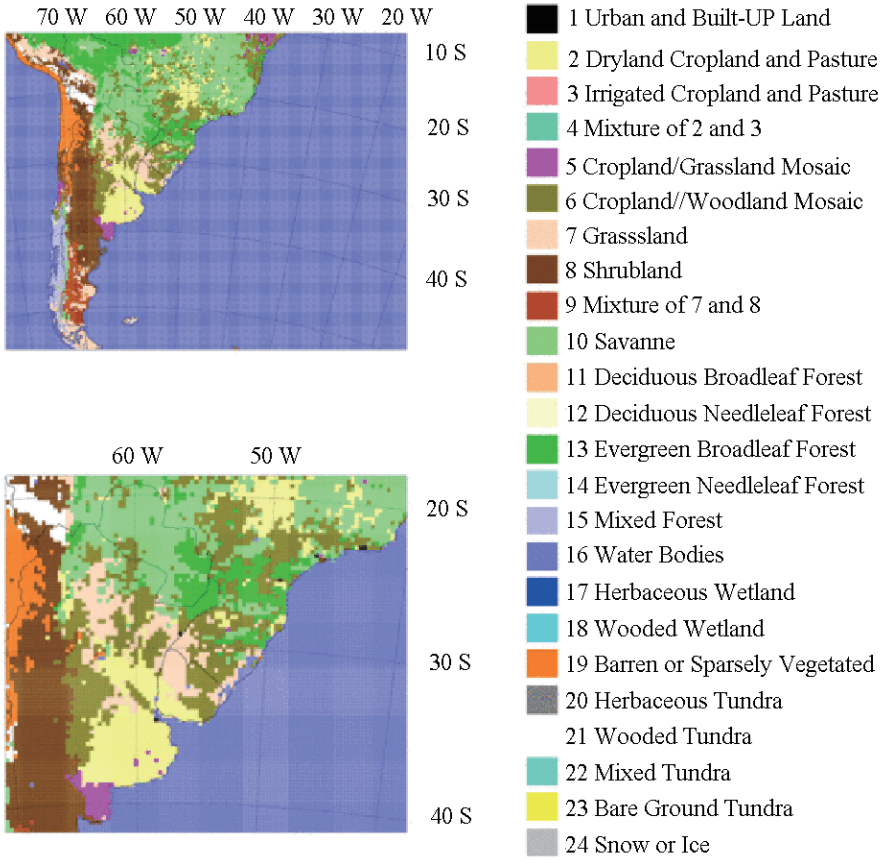

Fig. 2. Land-use/land-cover maps used for CNTL. Left panels show the mother and nested domains.

we used the 1982–1999 AVHRR-LTDR NDVI dateset following the approach described in Alvaraz-Segura et al. (2013). The 64 EFT types were not translated into the existing USGS categories; rather, the surface parameters were mapped to each EFT category for the period 1992–93 and converted to the format required in the WRF model. EFTs change from year to year, and so do their estimated surface parameters; inclusion of this fact was the main difference between this study and some previous studies (Kurkowski et al., 2003; Yucel, 2006).

Figure 2 displays the USGS land-cover map derived from the AVHRR data, for the 30-and 10-km model domains. The USGS terrestrial datasets with resolutions of 10′ and 5′ were used for the coarse and fine domains, respectively. In the figure, out of the 24 land-cover types, about 10 types can be seen in both domains; somewhat detailed land-cover distribution can be seen at a finer resolution. Figure 3 displays the median EFT map for the 1982–1999 period, derived from the LTDR-NDVI data, in the model domains. Unlike Fig. 2, all 64 EFT categories are seen in both domains, with larger (smaller) values indicating higher (lower) productivity of the surface vegetation.

WRF simulations were performed using two kinds of land-cover datasets. All simulations were conducted from 0000 UTC 1 September 1998 to 0000 UTC 1 December 1998, with NCEP/NCAR reanalysis data providing initial and 6-hourly boundary conditions. Experimental results for precipitation and 2-m air temperature were compared with the observational data. The control run (CNTL) represented the model simulation with the default USGS land-cover map (Fig. 2), which included various kinds of human-originated vegetation types(dry cropland, irrigated cropland, and their mixture) as well as natural vegetation (Savanna, evergreen broadleaf forest, and grasslands in the upper, middle, and lower parts of LPB, respectively).

In the experimental run (EFT), the 24 USGS land-cover types were replaced by the 64 EFTs shown in Fig. 3. In order to understand the changes to the mechanisms that induced precipitation, we examined the surface fluxes, near-surface temperature and winds, convective instability, and moisture transports feeding the region.

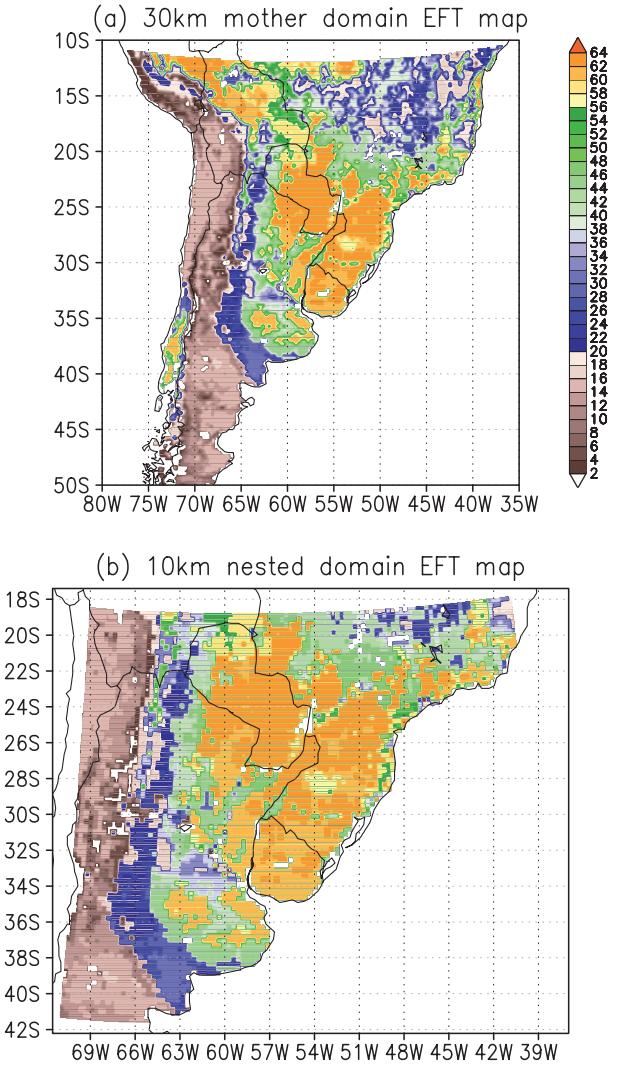

Fig. 3. The same as Fig. 2, but for EFT maps. Each of the 64 EFTs was assigned a code based on two letters and a number, i.e., 1: Aa1; 2: Aa2; 3: Aa3; 4: Aa4; 5: Ab1; ... ; 63: Dd3; and 64: Dd4. The first letter of the code (capital) corresponds to the NDVI mean level, ranging from A to D for low to high (increasing) productivity. The second letter (small) shows the seasonal coefficient of variation, ranging from a to d for high to low (decreasing) seasonality. The numbers indicate the season of maximum NDVI (1-4: spring, summer, autumn and winter).

2.3 *Observational data*

To evaluate the model's performance, independent measurements of precipitation were obtained from satellite estimates, specifically from the Tropical Rainfall Measurement Mission (TRMM; Kummerow et al., 1998) rainfall data. TRMM has a 3-hour time interval and a horizontal resolution of 0.25°×0.25°.

Given the emphasis of this research on surface processes, there was also interest in assessing the performance of the model's 2-m temperature. The monthly surface temperature dataset, at a horizontal resolution of 0.5°×0.5° (Brohan et al., 2006), from the Climate Research Unit (CRU) of the University of East Anglia was employed for this study. It is known that the region has a sparse observational network, and consequently the quality of this product remains to be

further assessed.

3. Effects of new land-cover data on the numerical model simulation

3.1 *Surface physical properties*

Figure 4 displays the surface albedo and roughness length fields in CNTL and their changes when using EFTs (EFT minus CNTL). Surface albedo was found to be low over evergreen broadleaf forest regions in the central LPB and the Amazonia (Fig. 4a). The albedo over the Andes mountains was 25% higher than that over the central LPB and Amazonia, with its maximum being located at a latitude of to 45°–50°S. In general, the characteristics of the surface roughness length were found to be opposite to those of albedo. The value of roughness over the evergreen broadleaf forest regions was observed to be higher than that over the other regions (Fig. 4c).

Hereafter, the analysis focused on the interior of the LPB, which is the study interest area. To simplify the analysis, two rectangle boxes were drawn in the panels: the upper box (28°–17°S, 66°–46°W) was called the "northern LPB" and the lower one (37°–28°S, 65°–51°W) the "southern LPB". The latitude 28°S was properly located so that the northern LPB contained areas in the central eastern LPB with increased albedo and decreased roughness length, while the southern LPB encompassed areas with decreased albedo and increased roughness length. We did not shrink the upper box to include the increased albedo and decreased roughness only, because we wanted the northern LPB to be covered as much as possible by the rectangular box, so that all areas of the basin could be mentioned. The same two boxes had also been used in the works of Lee and Berbery (2012). It can be seen that the maximum increase (decrease) in surface albedo (surface roughness) occurred in the northern LPB, while the maximum decrease (increase) in surface albedo (surface roughness) occurred in the southern LPB (Figs. 4b and d, respectively).

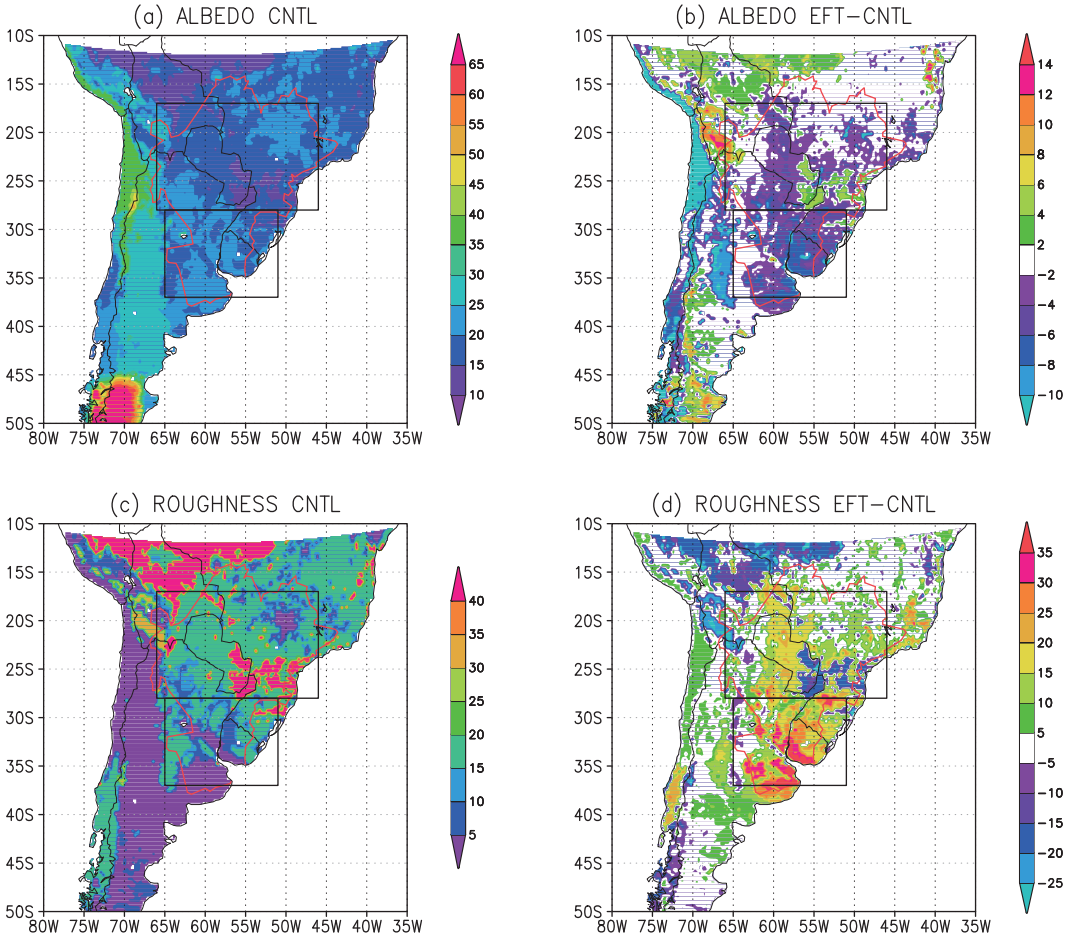

Fig. 4. Three-month (SON 1998) averaged (a) CNTL and (b) EFT minus CNTL fields for surface albedo (%). Parts (c) and (d) represent the same fields for surface roughness length (units: cm).

3.2 *Surface heat fluxes and near-surface atmospheric variables: 5-day running average*

Figures 5a and b present the time series of the differences (EFT minus CNTL) in the area-averaged surface heat fluxes over the two regions. In the northern LPB, the replacement of the USGS land-cover map by the EFTs led to a decrease in sensible heat fluxes, due to the increased surface albedo, and an increase in latent heat fluxes. The southern LPB exhibited opposite behavior in the sensible and latent heat fluxes time series, and the signal was relatively weak compared with the northern LPB.

Changes in the surface heat fluxes are expected to alter near-surface atmospheric variables. This can be seen in Figs. 5c and d, which represent the two area-averaged time series of the difference (EFT minus CNTL) in 2-m temperature and 2-m specific humidity. The decreased (increased) sensible heat fluxes

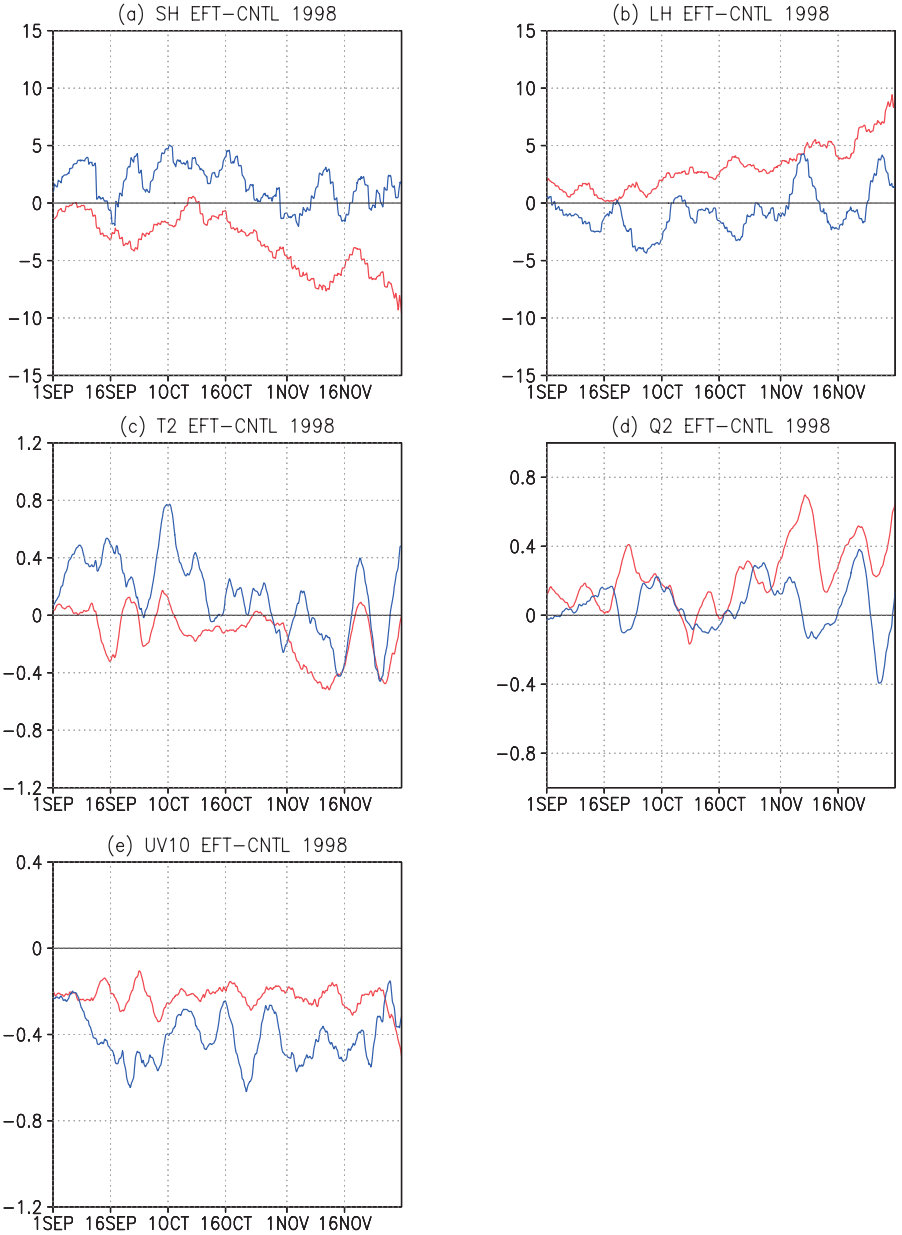

Fig. 5. Time series of (a) sensible heat fluxes (W m^{-2}), (b) latent heat fluxes (W m^{-2}), (c) 2-m temperature (°C), (d) 2-m water vapor mixing ratio (g kg^{-1}), and (e) 10-m wind speed (m s^{-1}). All are five-day running averaged, and the red (blue) colored line in parts (c) and (d) denotes the northern (southern) LPB.

in the northern (southern) LPB gave rise to a cooling of up to 0.5°C (a warming of below 0.8°C) near the surface (Fig. 5c). On the other hand, the increase in latent heat fluxes in the northern LPB was associated with an increase in specific humidity near the surface (Fig. 5d). In the southern LPB, the latent heat fluxes were reduced, but the corresponding 2-m specific humidity showed almost neutral changes because of its dependency on near-surface temperature and winds, in addition to latent heat fluxes.

Roughness length was reported to play a crucial role in determining near-surface wind direction and speed. The reduction of the roughness length in the northern LPB region gave rise to a reduction of 10-m wind speed in both the northern and the southern LPB regions (Fig. 5e). The maximum increase in surface roughness occurred in the southern LPB region; as a consequence a larger decrease in near-surface winds was reported in that region. The difference in wind speed was noted not to exceed 1 m s^{-1} in magnitude in an original time series without 5-day moving average, but the effect was consistent and lasted during most of the model integration process. The 3-month mean 10-m winds (Figs. 6a, c) showed strong easterly components in the CNTL simulation, especially along the eastern boundary of the basin. However, westerly-component winds were created by the use of EFTs, especially in the southern LPB (Figs. 6b, d). While the changes in near-surface winds were observed at a height of 10 m, they could modify, although slightly, the higher-level wind patterns.

3.3 *Local thermodynamic forcing*

The convective available potential energy (CAPE) and convective inhibition (CIN) are two important parameters that are widely used to analyze the local processes that account for the development of convective precipitation. CAPE (CIN) can be regarded as the

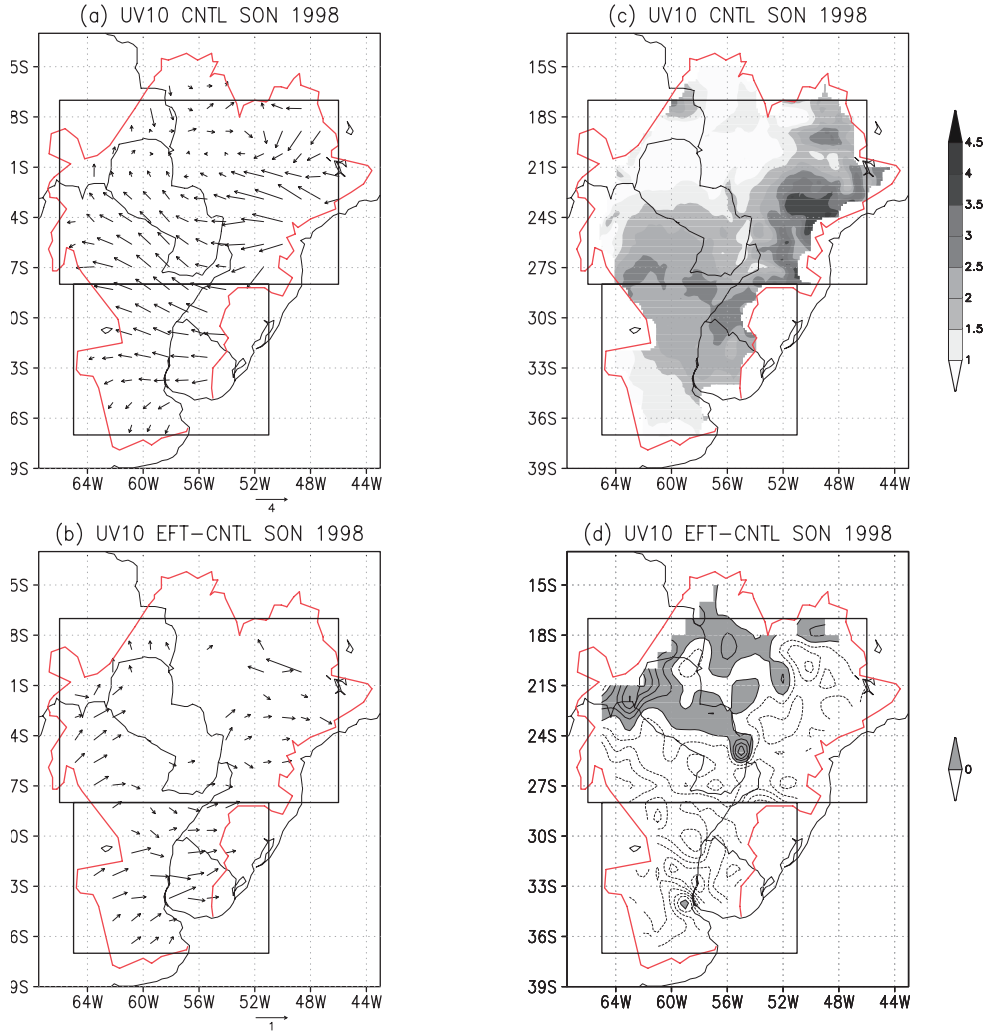

Fig. 6. Three-month (SON 1998) averaged (a) CNTL and (b) EFT minus CNTL for 10-m wind vector fields (m s^{-1}), and (c) CNTL and (d) EFT minus CNTL for 10-m wind speed; contour intervals in (d) are 0.1 m s^{-1}.

thermodynamic forcing facilitating (inhibiting) local convection and precipitation (Bluestein, 1993; Barlow et al., 1998). In this study, CAPE (CIN) was defined as the amount of positively (negatively) buoyant energy in the vertical sounding of temperature, so both have positive signs. To simplify the analysis, the maximum values from the vertical profile of CAPE and CIN at each horizontal point were used, which were named as MCAPE and MCIN, respectively.

Figure 7 displays the simulated 3-month average of the MCAPE and MCIN fields. It can be seen from Figs. 7a and b that in general there were relatively large MCAPE and MCIN over Paraguay in the CNTL. The increase in MCAPE in the northern LPB region was associated with an increase in the latent heat flux, as shown in Fig. 4b. The difference field (EFT minus CNTL) showed that use of the new land-cover map would increase MCAPE in the northern LPB region, including Paraguay, while decrease it slightly in the southern LPB (Fig. 7c). As shown in Fig. 7d, use of the new landscape data decreased MCIN in the southern LPB but had neutral impact in the northern LPB. Because large values of CAPE and small values of CIN are favorable conditions for local convection and precipitation, the increased CAPE over the northern LPB implies a higher possibility of the development of mesoscale convective systems in the region, especially around Paraguay.

3.4 *Large-scale horizontal moisture flows*

The local thermodynamic instability was not the only factor affecting precipitation in the LPB region. The change in precipitation was also a consequence of changes in moisture transport into the LPB. Such

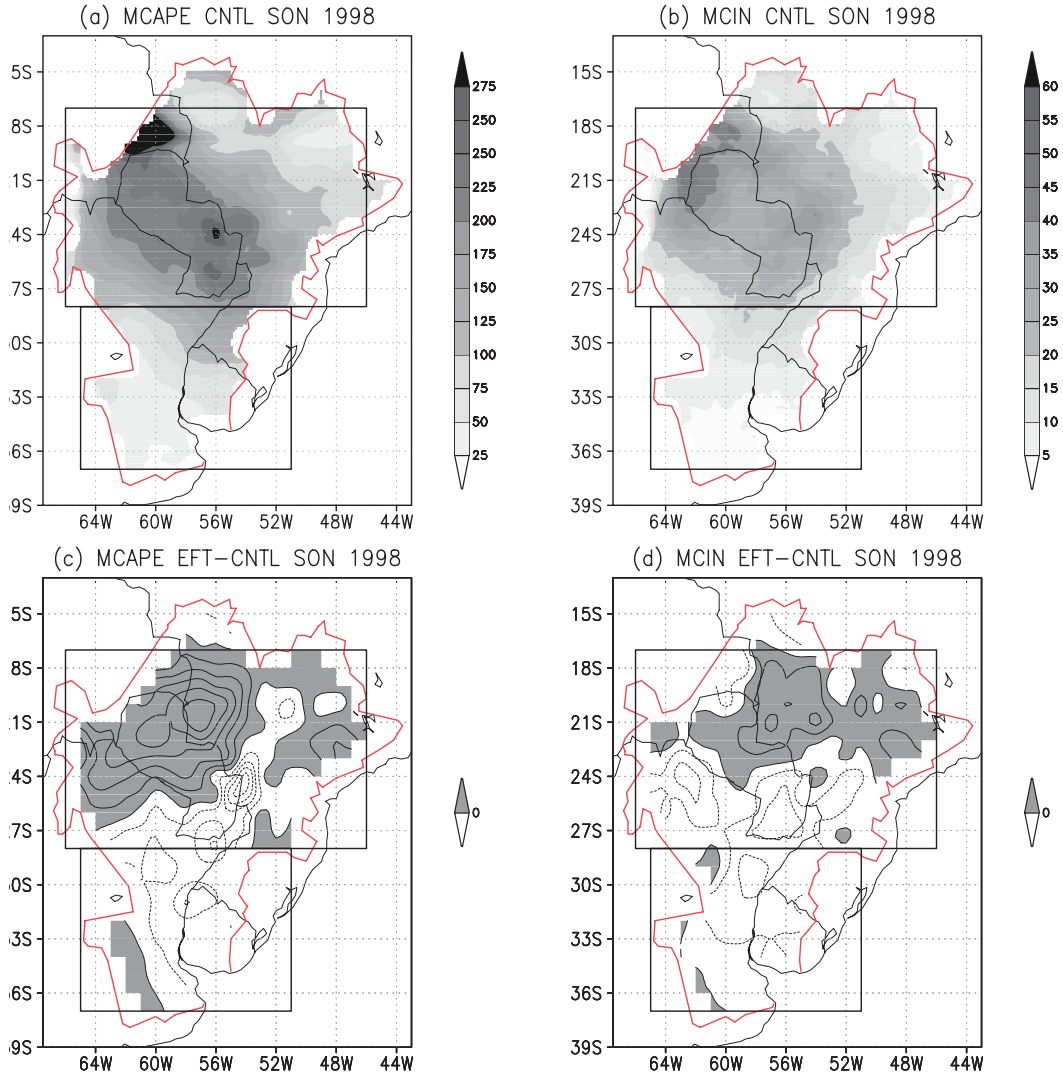

Fig. 7. Three-month (SON 1998) averaged CNTL for (a) maximum CAPE (MCAPE) and (b) maximum CIN (MCIN) (units: J kg^{-1}). Parts (c) and (d) represent EFT minus CNTL for MCAPE and MCIN, and contour intervals of 10 and 2 J kg^{-1}, respectively.

changes can be inferred based on the discussions in the previous section (Fig. 6) that the reduction of near-surface winds was expected to influence higher-level moisture flows and distributions.

Figure 8 displays the 3-month averaged moisture flux, vertically integrated from 1000 to 300 hPa, and the corresponding convergence and divergence fields. The CNTL (Fig. 8a) showed features that were consistent with previous climatologies derived from global reanalyses (Labraga et al., 2000; Berbery and Barros, 2002; Doyle and Barros, 2002; Marengo et al., 2004), and with month- or season-long simulations (Collini et al., 2008; Lee and Berbery, 2012). The northwestern LPB, including Bolivia and Paraguay, exhibited a large southeastward moisture transport (Fig. 8b), supplying moisture into the LPB from the Amazon basin.

As can be seen from Figs. 8c and d, use of the new land-cover map modified regional moisture transports. From Fig. 8c, it is clear that westerly moisture flows were produced in the southern LPB and most of them turned toward north in the northern LPB. Some of the westerly moisture maintained an eastward flow and created relatively small perturbations in moisture fluxes over the South Atlantic Ocean. The Brazilian Highlands seemed to play an important role in the splitting of the westerly moisture flow. The westerly (southerly) moisture fluxes in the southern (northern) LPB produced convergence of moisture flux in the southern LPB (Fig. 8d). In the northern LPB, both moisture flux convergence and moisture flux divergence occurred, but on average moisture flux convergence was slightly larger, with its maximum being located in northern Paraguay. All these features suggest that precipitation in the southern LPB would have been supported mainly by the large-scale moisture flux convergence rather than by local thermodynamic forcing.

3.5 *Precipitation*

Figures 9a and b display the 3-month averaged total precipitation in CNTL and the difference (EFT minus CNTL). The CNTL precipitation field showed

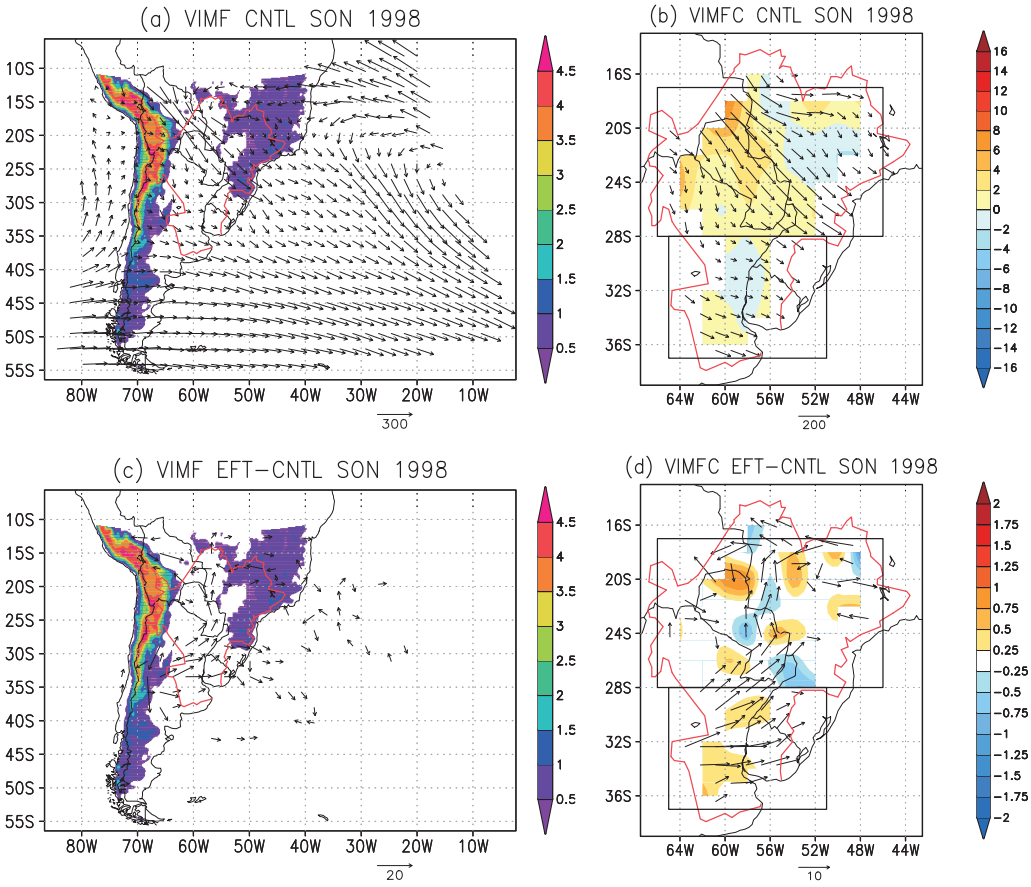

Fig. 8. Three-month (SON 1998) averaged CNTL for (a) vertically integrated moisture fluxes in kg (m s)$^{-1}$ and (b) their convergence (mm d^{-1}). Parts (c) and (d) represent, respectively, the fluxes and their convergence for EFT minus CNTL. Shaded areas in (a) and (c) are model terrain height (km), and the moisture flux convergence (divergence) is positive (negative) in (b) and (d).

overall consistency with the vertically integrated moisture flux convergence and divergence fields (Fig. 8b) in both the northern and the southern LPB regions. The regions of increased (decrease) precipitation were collocated with vertically integrated moisture flux convergence (divergence). The difference field (Fig. 9b) also corresponded well to the moisture flux convergence field (Fig. 8d). On the other hand, similar comparisons in case of the MCAPE difference field (Fig. 7c) showed a good correspondence over the northern LPB but not for the southern LPB portion.

The difference in total precipitation (Fig. 9b) between CNTL and EFT can be understood as the combined effects of both local (subsection 3.3) and large-scale (subsection 3.4) forcing induced by the use of the new land-cover map. Figures 9c and d display area-averaged time series of the difference (EFT minus CNTL) in convective and nonconvective precipitations over the northern and southern LPB regions. The precipitation type in northern LPB was clearly different from that in the southern LPB. The northern LPB exhibited increases in both convective and nonconvective precipitations with time. The southern LPB showed an increase in nonconvective precipitation similar to that in case of the northern LPB, but almost no change in convective precipitation. This means that, the use of new land-cover map increased both local thermodynamic and large-scale dynamic forcing in the northern LPB, while only a large-scale dynamic forcing increased in the southern LPB.

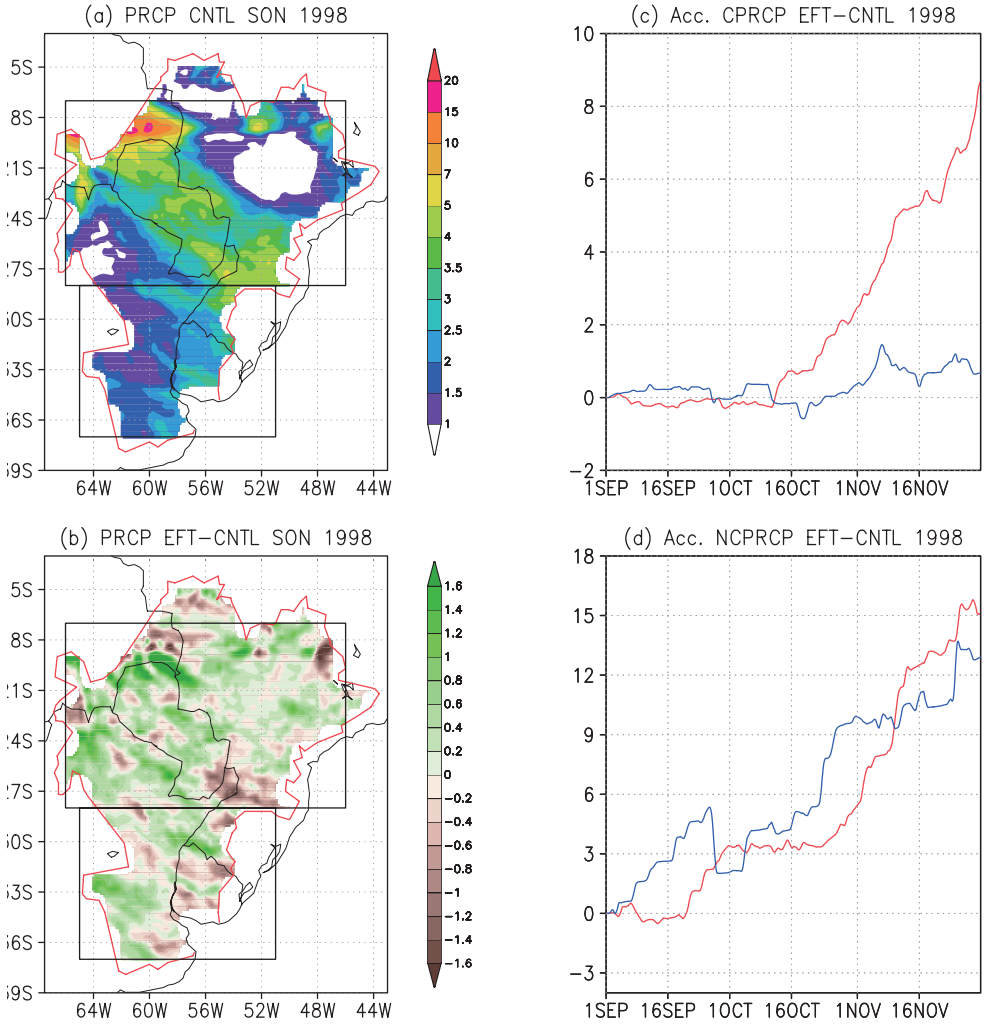

Fig. 9. Three-month (SON 1998) averaged (a) CNTL and (b) EFT minus CNTL for surface precipitation (mm d^{-1}). Time series of 3-month averaged fields of the difference (EFT minus CNTL) in (c) convective precipitation and (d) nonconvective precipitation (units: mm d^{-1}). All are 5-day running averaged, and the red (blue) colored line in (c) and (d) denotes the northern (southern) LPB.

4. Comparison with observations

Figure 10 shows the time series of simulated minus observed total accumulated precipitation over the LPB during the austral spring of 1998. Overall, the CNTL showed smaller-than-observed precipitations, except in September. The difference between CNTL and observed precipitations became clearer with time, reaching about 20–30 mm by the end of November. However, use of the EFT data in the model increased accumulated precipitation, and the gap between EFT and CNTL data increased with time. This implies that use of the new land-cover map can reduce biases in precipitation, which are relevant for the warmer season, with the potential improvement of summer season precipitation.

Figure 11 displays the 1-month averaged precipita-

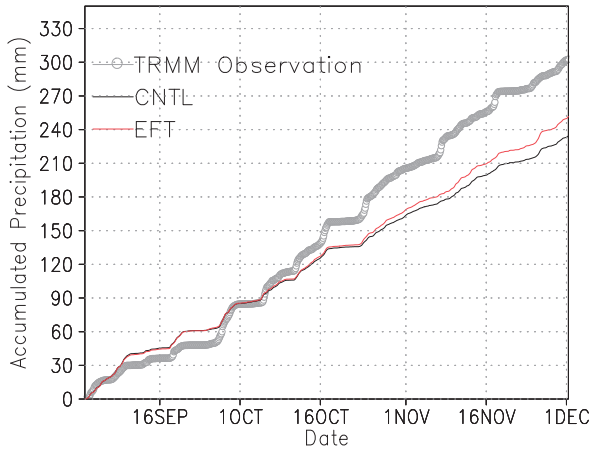

Fig. 10. Time series of observed, CNTL, and EFT accumulated precipitations (mm).

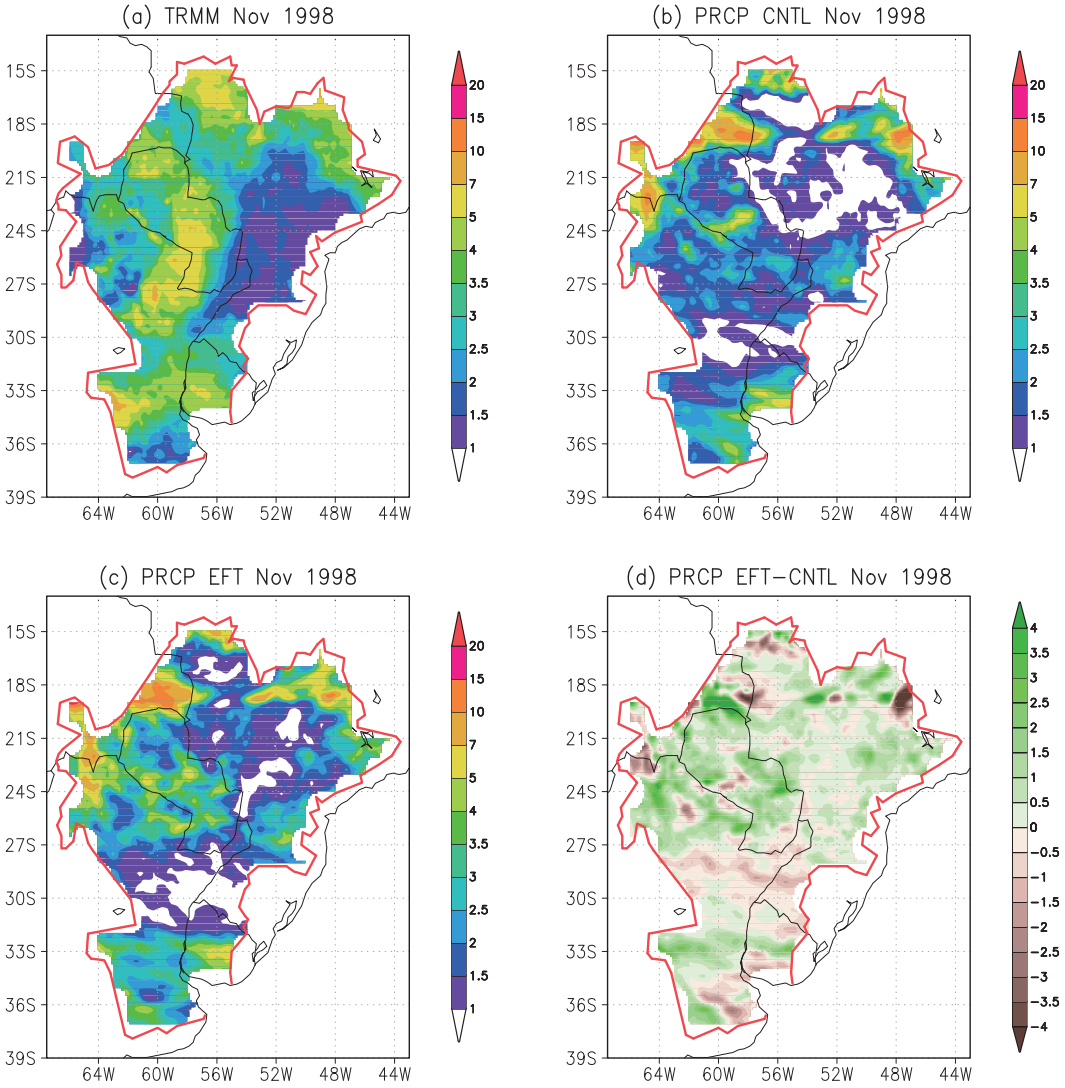

Fig. 11. Averaged precipitation (mm d^{-1}) in November 1998 for (a) observation, (b) CNTL, (c) EFT, and (d) EFT minus CNTL.

tion for November 1998. First, with the introduction of the new land-cover data, the areas of total precipitation increased by over 1 mm in the interior LPB. Also, the horizontal distribution of precipitation was improved substantially and the magnitude of precipitation was closer to the TRMM observation data.

Figures 12a and b display 3-month averaged field of observed and simulated 2-m temperature, respectively. The observations showed maximum temperatures around 18°S in latitude and gradients in the northeast–southwest directions (Fig. 12a). The CNTL simulation reproduced such patterns well and, in general, showed reasonable consistency with the spatial distribution of observed temperature. Figure 12c displays the difference between CNTL and observation data. The CNTL simulation tended to have cold biases along the boundary of the LPB, while having warm biases in southern Paraguay and north of Paraguay (Fig. 12c). As can be seen from Fig. 12d, the warm bias over the southern Paraguay and the cold bias over Uruguay were reduced with the use of the new land-cover map.

Temperature-measuring stations are even sparser than the precipitation-measuring ones, and this dataset might have unreliable values over large ungauged regions; thus, the evaluation should not be more than qualitative. In order to see how monthly mean error of the 2-m temperature evolves with time, biases in 2-m temperature were calculated in the rectangular box denoting low-altitude regions within the

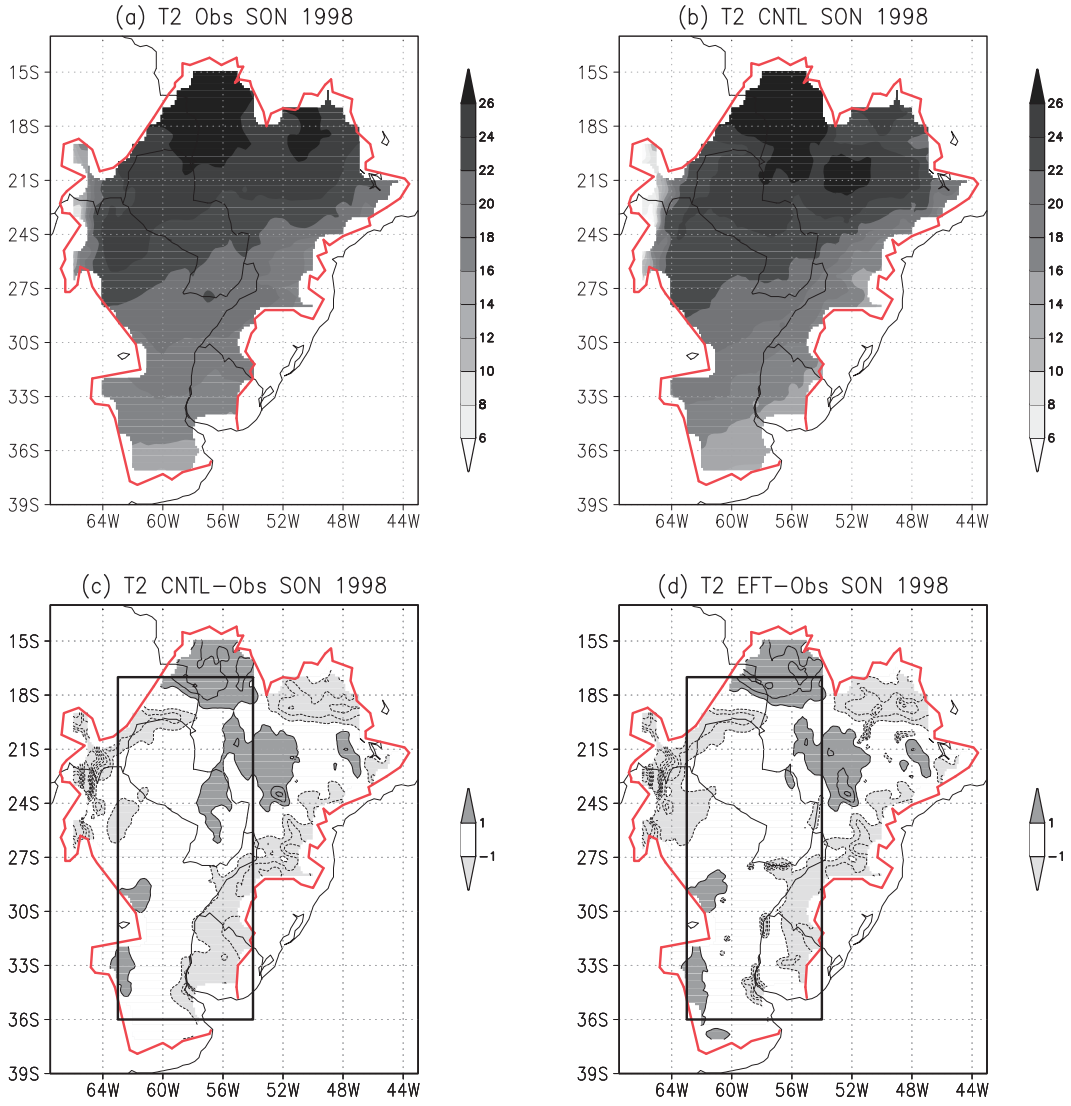

Fig. 12. Three-month (SON 1998) averaged 2-m air temperature (°C) for (a) observation, (b) CNTL, (c) CNTL minus observation, and (d) EFT minus observation.

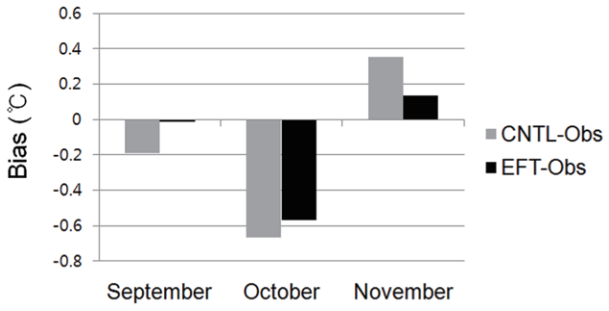

Fig. 13. Biases in the 2-m temperature (°C) over the box area in Fig. 12d for each month during SON 1998.

LPB, which were considered to exhibit better-quality observations than the mountainous regions within the basin. Figure 13 shows the difference between simulated and observed mean 2-m temperatures over the low-altitude region for each month in the austral spring of 1998. All the 3 months had biases ranging from about −0.7°C to 0.4°C, with October showing the largest difference among them. The CNTL run had negative differences in the first two months and positive difference afterward. The biases of the EFT run were of the same sign as, but smaller amplitude than, those of CNTL in all the 3 months. Use of EFT data instead of USGS data in the model reduced biases in monthly mean 2-m temperature over the LPB by 54% (an average of 89%, 14%, and 60% for the three months) in spring 1998. However, as these results were based on single simulations, the statistical significance could not be determined, and thus they should be considered preliminary.

5. Summary and conclusions

Accurate specification of the land-surface states is important in numerical weather and climate prediction, and simulation studies in general. Recent efforts have focused on substituting the existing ground-based land-cover data, which are estimated by a multiyear climatology, with satellite-based land-cover data in numerical models. Those efforts were realized in state-of-the-art numerical models. Typically, ground-based and satellite-derived datasets use structural classifications of vegetation, and are insensitive to rapid and complex environmental changes.

In this paper, a new concept of a functional land-cover classification (EFTs) was introduced in a numerical mesoscale model. The EFTs are patches of the land surface with similar carbon gain dynamics and consist of 64 functional categories of vegetation. A surface physical parameter set, linked with each EFT, was incorporated into the model without mapping to existing structural categories. The effect of this incorporation on model simulations was investigated at the LPB region in South America for the austral spring of 1998.

Compared with the existing USGS land-cover dataset, the use of the new dataset showed substantial changes in surface albedo and roughness length fields. Such changes were found to modify surface fluxes and near-surface atmospheric variables, resulting in changes in local thermodynamic forcing and large-scale moisture flow patterns.

Through comparisons with observations, it was found that the use of the new data improved model performance for precipitation and 2-m temperature simulations in terms of magnitude and spatial distribution. These encouraging first results indicate the importance of the EFT information and the need for weather and climate models to incorporate, in some form, the functional changes in vegetation properties to increase the accuracy of forecasts and simulations. The results reported here are based on limited simulations to present alternative ways of representing the surface parameters, but more work needs to be done to confirm the robustness of the results. As presented, these results should be viewed as a proof of concept rather than as definitive conclusions. It remains for subsequent studies to investigate whether this improvement for the austral spring of 1998 is true for other seasons and years.

Acknowledgements. We are grateful to two anonymous reviewers for many valuable comments. This research was supported by the Korea Meteorological Administration Research and Development Program under Grant CATER 2012–3030. This research was supported by NASA Grant NNX08AE50G, NOAA Grant NA09OAR4310189, and the Inter American Institute for Global Change Research (IAI) through the Cooperative Research Network (CRN)-2094.

REFERENCES

Alcaraz-Segura, D., J. M. Paruelo, H. E. Epstein, and J. Cabello, 2013: Environmental and human controls of ecosystem functional diversity in temperate South America. *Remote Sensing*, **5**, 127–154.

Anderson, J. R., E. E. Hardy, J. T. Roach, and R. E. Witmer, 1976: A land use and land cover classification system for use with remote sensor data. U.S. Geological Survey Professional Paper 964, 28pp.

Barlow, M., S. Nigam, and E. H. Berbery, 1998: Evolution of the North American monsoon system. *J. Climate*, **11**, 2238–2257.

Berbery, E. H., and V. R. Barros, 2002: The hydrologic cycle of the La Plata basin in South America. *J. Hydrometeorology*, **3**, 630–645.

Bluestein, H. B., 1993: *Synoptic–Dynamic Meteorology in*

Midlatitudes. Vol. 2, Oxford University Press, 594pp.

Brohan, P., J. J. Kennedy, I. Harris, S. F. B. Tett, and P. D. Jones, 2006: Uncertainty estimates in regional and global observed temperature changes: A new dataset from 1850. *J. Geophys. Res.*, **111**, D12106, doi: 10.1029/2005JD006548.

Chen, F., and J. Dudhia, 2001: Coupling an advanced land-surface/ hydrology model with the Penn State/ NCAR MM5 modeling system. Part I: Model description and implementation. *Mon. Wea. Rev.*, **129**, 569–585.

Collini, E. A, E. H. Berbery, V. R. Barros, and M. E. Pyle, 2008: How does soil moisture influence the early stages of the South American monsoon? *J. Climate*, **21**, 195–213.

Doyle, M. E., and V. R. Barros, 2002: Midsummer low-level circulation and precipitation in subtropical South America and related sea surface temperature anomalies in the South Atlantic. *J. Climate*, **15**, 3394–3410.

Dudhia, J., 1989: Numerical study of convection observed during the winter monsoon experiment using a mesoscale two-dimensional model. *J. Atmos. Sci.*, **46**, 3077–3107.

Hong, S.-Y., and J.-O. J. Lim, 2006: The WRF single-moment 6-class microphysics scheme (WSM6). *J. Korean Meteor. Soc.*, **42**, 129–151.

Janjić, Z. I., 1990: The step-mountain coordinate: Physical package. *Mon. Wea. Rev.*, **118**, 1429–1443.

Janjić, Z. I., 1994: The step-mountain eta coordinate model: Further developments of the convection, viscous sublayer and turbulence closure schemes. *Mon. Wea. Rev.*, **122**, 927–945.

Janjić, Z. I., 1996: The surface layer in the NCEP Eta Model. Preprints, *Eleventh Conf. on Numerical Weather Prediction*, Norfolk, VA, Amer. Meteor. Soc., 354–355.

Janjić, Z. I., 2000: Comments on "Development and evaluation of a convection scheme for use in climate models". *J. Atmos. Sci.*, **57**, 3686.

Janjić, Z. I., 2002: Nonsingular Implementation of the Mellor–Yamada Level 2.5 Scheme in the NCEP Meso model. NCEP Office Note, No. 437, 61 pp.

Kalnay, E., and Coauthors, 1996: The NCEP/NCAR 40-Year Reanalysis Project. *Bull. Amer. Meteor. Soc.*, **77**, 437–471.

Kummerow, C., W. Barnes, T. Kozu, J. Shiue, and J. Simpson, 1998: The tropical rainfall measuring mission (TRMM) sensor package. *J. Atmos. Oceanic Technol.*, **15**, 809–817.

Kurkowski, N. P., D. J. Stensrud, and M. E. Baldwin, 2003: Assessment of implementing satellite-derived land cover data in the Eta model. *Wea. Forecasting*, **18**, 404–416.

Labraga, J. C., O. Frumento, and M. Lopez, 2000: The atmospheric water vapor cycle in South America and the tropospheric circulation. *J. Climate*, **13**, 1899–1915.

Lee, S.-J., 2010: Impact of land surface vegetation change over the La Plata Basin on the regional climatic environment: A study using conventional land-cover/land-use and newly developed ecosystem functional types. Ph.D. dissertation, University of Maryland, 153pp.

Lee, S.-J., and E. H. Berbery, 2012: The impact of land-use and land-cover changes on the climate of the La Plata Basin. *J. Hydrometeorology*, **13**, 84–102.

Loveland, T. R., and A. S. Belward, 1997: The IGBP-DIS global 1-km land cover data set, DISCover: First results. *Int. J. Remote Sens.*, **18**, 3291–3295.

Marengo, J. A., W. R. Soares, C. Saulo, and M. Nicolini, 2004: Climatology of the low-level jet east of the Andes as derived from the NCEP-NCAR reanalyses: Characteristics and temporal variability. *J. Climate*, **17**, 2261–2280.

Michalakes, J., S. Chen, J. Dudhia, L. Hart, J. Klemp, J. Middlecoff, and W. Skamarock, 2001: Development of a Next Generation Regional Weather Research and Forecast Model. *Developments in Teracomputing: Proc. the Ninth ECMWF Workshop on the Use of High Performance Computing in Meteorology,* W. Zwieflhofer and N. Kreitz, Eds., World Scientific, 269–276.

Mlawer, E. J., S. J. Taubman, P. D. Brown, M. J. Iacono, and S. A. Clough, 1997: Radiative transfer for inhomogeneous atmosphere: RRTM, a validated correlated-k model for the longwave. *J. Geophys. Res.*, **102** (D14), 16663–16682.

Paruelo, J. M., E. G. Jobbagy, and O. E. Sala, 2001: Current distribution of ecosystem functional types in temperate South America. *Ecosystems*, **4**, 683–698.

Yucel, I., 2006: Effects of implementing MODIS land cover and albedo in MM5 at two constrasting U.S. Regions. *J. Hydrometeorology*, **7**, 1043–1060.